**ORIGINAL PAPER**

# Characterizing Fracturing of Clay-Rich Lower Watrous Rock: From Laboratory Experiments to Nonlocal Damage-Based Simulations

N. Guy[1,2,4] · D. M. Seyedi[1,3] · F. Hild[4]

## Abstract
The work presented herein aims at characterizing and modeling fracturing (i.e., initiation and propagation of cracks) in a clay-rich rock. The analysis is based on two experimental campaigns. The first one relies on a probabilistic analysis of crack initiation considering Brazilian and three-point flexural tests. The second one involves digital image correlation to characterize crack propagation. A nonlocal damage model based on stress regularization is used for the simulations. Two thresholds both based on regularized stress fields are considered. They are determined from the experimental campaigns performed on Lower Watrous rock. The results obtained with the proposed approach are favorably compared with the experimental results.

**Keywords** Crack network · Fracture toughness · Nonlocal damage · Rock fracturing · Weibull model

## List of Symbols

| | |
|---|---|
| $\sigma$ | Stress tensor |
| $\overline{\sigma}$ | Regularized stress tensor |
| $\ell_c$ | Characteristic length |
| $\Delta$ | Laplacian operator |
| $n$ | Normal to surface |
| $P_i$ | Crack initiation probability |
| $S_i$ | Crack initiation stress |
| $\frac{\sigma_0^m}{\lambda_0}$ | Scale parameter |
| $V_{el}$ | Volume of an element |
| $m$ | Weibull modulus |
| $\sigma_{\ell_c}$ | Nominal stress |
| $S_g$ | Crack growth stress |
| $K_c$ | Fracture toughness |
| $\Gamma$ | Gamma function |
| $\rho$ | Mass density |
| $d$ | Damage |
| $\psi_e$ | State potential |
| $\mathcal{C}$ | Hooke's tensor |
| $\epsilon$ | Infinitesimal strain tensor |
| $Y$ | Thermodynamic force associated with damage |
| $H_e$ | Heaviside function |
| $\overline{\sigma}_I$ | Maximum principal regularized stress |
| $a$ | Half-length of critical defect |
| $\sigma_w$ | Weibull stress |
| $\sigma_{wi}$ | Weibull stress associated with sample $i$ |
| $P_F$ | Failure probability |
| $P_{Fi}$ | Failure probability associated with sample $i$ |
| $\sigma_f$ | Critical maximum principal stress |
| $H$ | Stress heterogeneity factor |
| $V$ | Sample volume |
| $H_{br}$ | Stress heterogeneity factor for Brazilian test |
| $V_{br}$ | Sample volume for Brazilian test |
| $H_{fl}$ | Stress heterogeneity factor for three-point flexural test |
| $V_{fl}$ | Sample volume for three-point flexural test |
| $n_s$ | Total number of samples |
| $R$ | Radius of Brazilian test sample |
| $L$ | Length of Brazilian test sample |
| $K_I$ | Mode I stress intensity factor |
| $K_{II}$ | Mode II stress intensity factor |
| $r_K$ | Ratio between mode II and mode I stress intensity factors |

✉ N. Guy
nicolas.guy@ifpen.fr

1. BRGM, Natural Risks and CO2 Storage Safety Division, 3 Avenue Claude Guillemin, BP36009, 45060 Orléans, France

2. Present Address: IFP Energies Nouvelles, 1 & 4 Avenue Bois-Préau, 92852 Rueil-Malmaison Cedex, France

3. Present Address: Andra, R & D Division, 1-7 rue Jean Monnet, 92290 Chatenay-Malabry, France

4. LMT, ENS Paris-Saclay / CNRS / Université Paris-Saclay, 61 Avenue du Président Wilson, 94235 Cachan Cedex, France

# 1 Introduction

The characterization and modeling of damage and cracking in quasi-brittle materials such as concrete and rocks is of great interest in different engineering applications such as deep geothermal energy production, $CO_2$ geological storage, nuclear waste underground disposal or for unconventional oil and gas production. Such applications require an accurate description of fracturing of geological formations to characterize structure stability and rock strength (Funatsu et al. 2004). Furthermore, characterizing rock fracturing can also be a key issue to evaluate induced changes in flow properties (Baghbanan and Lanru 2007; Jobmann et al. 2010) such as permeability and fracturing-induced leakage or pressure modification.

Damage, cracking and rock fracturing are based on two key phenomena, namely crack initiation and propagation. The description of crack propagation in quasi-brittle materials remains a challenging task despite important efforts carried during past decades. In numerical simulations with standard (i.e., local) softening damage models the strain field localizes in a band with a thickness of one element (Pietruszczak and Mróz 1981). The results exhibit a pathological dependence on the spatial discretization, namely the mesh fineness and the orientation of elements. As an extreme case, it can be shown that for a very fine discretization the predicted fracture energy approaches zero (Pietruszczak and Mróz 1981; Bažant and Belytschko 1985), which is unrealistic from a physical point of view. The loss of ellipticity of the equations describing the mechanical problem has been identified as the corresponding mathematical issue (Triantafyllidis and Aifantis 1986; Lasry and Belytschko 1988; De Borst et al. 1993). Different regularization schemes have been proposed to avoid the ill-posedness of the mathematical description at a certain level of accumulated damage. Nonlocal damage models (Pijaudier-Cabot and Bažant 1987; Bažant and Pijaudier-Cabot 1988) provide a suitable framework to have mesh objective results when dealing with the post-localized behavior. Higher-order strain (Peerlings et al. 1998; Lorentz and Benallal 2005), stress (Guy 2010; Guy et al. 2012) or damage (Lyakhovsky et al. 2011) gradients are used to include a nonlocal effect, thus removing the sensitivity of the model to spatial discretization.

Moreover, geomaterials commonly exhibit large scatter on their mechanical parameters because of their natural components. Regarding clay-rich rocks, this heterogeneity may come from the variability of the mineral composition of the rock, *e.g.,* the clay content or the presence of flaws. Crack initiation in rocks usually has a random character with a scatter in initiation stress. The effect of this randomness on the cracking probability needs to be taken into account in both material behavior characterization and modeling (Guy et al. 2010). This heterogeneity can be evaluated experimentally considering a relevant number of specimens, performing systematic failure tests and using an appropriate approach to analyze the results such as the methods proposed by Weibull (1939), and completed by the work of Beremin (1983) and Da Silva et al. (2004). Furthermore, the experimental identification of parameters describing crack propagation in quasi-brittle and heterogeneous material leads to specific challenges because of their brittleness. Several specific experimental procedures have been developed (Zuo et al. 2014) such as straight edge cracked round bar bend (SECRBB; Bush 1976) or chevron bend (CB; Ouchterlony 1988) tests. Another test allowing a rock specimen to be pre-cracked without leading to brittle failure is the so-called sandwiched beam (SB; Pancheri et al. 1998] configuration. With this method, crack propagation is controlled and therefore quantified before encountering specimen failure.

A complete study of rock fracturing from laboratory test to numerical modeling is presented in this paper. It is based on original experimental results and new validations of the numerical model introduced by the present authors. The latter is a nonlocal damage model using two thresholds based on a regularized stress field (Guy et al. 2012). Each threshold is associated with a cracking regime. Crack initiation is characterized through a probabilistic analysis based on three-point flexural and Brazilian tests. Crack propagation is analyzed through SB tests with digital image correlation (Roux and Hild 2006). In order to evaluate the relevance of the results obtained with the numerical model, the tests are simulated using the identified parameters.

# 2 Probabilistic Nonlocal Model for Rock Fracturing

The heterogeneity in rocks is always at the origin of the scatter observed in the measured failure stress of samples (Baecher and Einstein 1981). The rock mass heterogeneity will be described by the presence of defects with a random distribution. The scatter of failure stress for rocks is explained by the presence of microcracks (i.e., initial defects) that are at the origin of crack initiation, causing its subsequent failure. A probabilistic model based on a Poisson point process is used to describe this random character by relating the material microstructure and its macroscopic behavior. In the present work a probabilistic nonlocal model (Guy 2010; Guy et al. 2012) is used to study possible cracking of the rock mass due to stress changes. Two different thresholds are considered for crack initiation and propagation. A damage threshold based on the Weibull (1939) model is used to account for the stochastic nature of crack initiation(s) and

then a fracture-mechanics-based threshold to model crack propagation. Both thresholds are probed by using a regularized stress field to avoid mesh dependency and localization phenomena. The regularization operation is performed over a characteristic length $\ell_c$ that must be long enough with respect to the size of the elements in the zone of interest. In the present case, it is proposed to choose the characteristic length equal to the largest defect size. This choice provides a crack initiation threshold greater than or equal to the crack growth threshold. The characteristic length thus stands for a microstructural parameter that is the size of the largest initial crack modeled as a defect. The bigger cracks can be modeled as a set of completely damaged elements. The regularization operator reads

$$\overline{\sigma} - \ell_c^2 \Delta \overline{\sigma} = \sigma, \ \left( \nabla \overline{\sigma} \right) \cdot n = 0 \tag{1}$$

where $\overline{\sigma}$ is the regularized stress tensor and $\sigma$ the Cauchy stress tensor. The vector $n$ is normal to a surface where natural boundary conditions are considered. The used procedure is similar to the implicit gradient enhanced scheme proposed by Peerlings et al. (1998, 2001).

Let us consider the case of crack initiation under tensile stresses, i.e., in mode I. In this setting, the initiation of new macrocracks follows the weakest link assumption and a Weibull model can explain the scatter of the experimental results. An initiation probability $P_i(el) \in [0;1]$ calculated from a uniform distribution is assigned to each sub-domain (i.e., each element). An initiation stress is then calculated for each sub-domain from an inverse Weibull law

$$S_i(el) = \frac{\sigma_0}{\left(\lambda_0 V_{el}\right)^{\frac{1}{m}}} \left[ -\ln \left( 1 - P_i(el) \right) \right]^{\frac{1}{m}} \tag{2}$$

where $V_{el}$ is the volume of the considered element, $m$ the Weibull modulus, and $\frac{\sigma_0^m}{\lambda_0}$ the scale parameter. A crack will initiate in the considered element if the regularized maximum principal stress reaches $S_i(el)$. The initiated macrocracks are assumed to be perpendicular to the regularized maximum principal stress direction. For a given characteristic length, a nominal stress is defined as

$$\sigma_{\ell_c} = \sigma_0 / \left( \lambda_0 \ell_c^3 \right)^{1/m} \tag{3}$$

which is useful to obtain an estimation of the stress state associated with crack initiation. It corresponds to the necessary loading leading to initiate a crack in a loaded element of volume $\ell_c^3$ with a probability of $1 - 1/e \approx 0.63$. Considering the two-dimensional case of a crack in an elastic medium submitted to a far field loading, the asymptotic Westergaard solution (Kanninen et al. 1982) gives a good approximation of the stress field around the crack tip. Considering Eq. (1) as a nonhomogeneous Helmholtz equation, the proposed

operator provides a regularized stress field in the vicinity of the crack tip corresponding to Westergaard asymptotic solution. The present procedure allows the stress intensity factor to be calculated without any mesh refinement for a propagating crack. Therefore, a direct transition from a damage-mechanics-based model for crack initiation to a fracture-mechanics-based model for crack propagation is provided. In addition, both models use the same variable, i.e., the regularized stress. In this framework the crack propagation threshold reads

$$S_g(el) = \frac{6\Gamma^2 \left( \frac{3}{4} \right)}{5\pi} \frac{K_c}{\sqrt{\pi \ell_c}} \tag{4}$$

where $K_c$ is the fracture toughness of the rock and $\Gamma$ the Gamma function. For a mode I crack, the above-mentioned criterion tends to a fracture mechanics threshold for an open crack when the characteristic length $\ell_c$ becomes small compared with the macroscopic scale. It is to be noted that the introduced criterion accounts for mixed-mode propagation

$$K_c \leq \frac{5K_I + \sqrt{K_I^2 + 16K_{II}^2}}{6} \approx K_I + \frac{2}{3}K_{II} \tag{5}$$

where $K_I$ and $K_{II}$ stand for the mode I and II stress intensity factors, respectively. A perfectly brittle behavior of an isotropic material is considered as a local damage law. The Helmholtz state potential thus reads

$$\rho \psi_e = \frac{1}{2}(1 - d) \epsilon \, C \, \epsilon \tag{6}$$

where $C$ is Hooke's tensor of the virgin material, $\rho$ the mass density, $\epsilon$ the infinitesimal strain tensor, and $d$ the damage variable. From the state potential, the stress–strain relationship is obtained

$$\sigma = \rho \frac{\partial \psi_e}{\partial \epsilon} = (1 - d)C \, \epsilon. \tag{7}$$

In this framework the non-damaged medium is considered as having a linear elastic behavior, which is a simplifying assumption as viscosity may influence both long-term relaxation and short-term dissipation, thereby stabilizing dissipation and damage growth especially for unstable crack propagation (Lyakhovsky et al. 2011). These effects are not considered herein for the sake of simplicity since the study focuses on stable crack propagation under mechanical loadings that do not involve significant strain due to long-term relaxation. The thermodynamic force associated with the damage variable $d$ is defined as

$$Y = -\rho \frac{\partial \psi_e}{\partial d} = \frac{1}{2} \epsilon \, C \, \epsilon. \tag{8}$$

Damage growth is written as

$$d = H_e\left(\langle \overline{\sigma}_I - S_i \rangle + \langle \overline{\sigma}_I - S_g \rangle\right) \quad \text{when } \dot{d} \geq 0 \tag{9}$$

where $H_e$ denotes the Heaviside step function, $\overline{\sigma}_I$ the maximum principal regularized stress, $S_i$ and $S_g$ the initiation and propagation thresholds.

The crack initiation criterion is introduced considering that a crack initiation stress is associated with each initial defect. The initial defects greater than $2\ell_c$ cannot be considered in this way. Let us consider a domain with a critical defect of half-length $a$. Assuming that the characteristic length is greater than $a$ leads to

$$S_i = \frac{K_c}{\sqrt{\pi a}} \geq \frac{K_c}{\sqrt{\pi \ell_c}} > \frac{6\Gamma\left(\frac{3}{4}\right)}{5\pi} \frac{K_c}{\sqrt{\pi \ell_c}} = S_g. \tag{10}$$

A characteristic length greater than the size of the largest initial defect provides a crack initiation threshold greater than the propagation threshold. The characteristic length corresponds to a microstructural parameter that is the size of the largest initial crack modeled as a defect. Initial cracks of size larger than $2\ell_c$ can be modeled as a set of completely damaged elements.

## 3 Characterization of Rock Fracturing

In this section, the consistency of both experimental and numerical results provided by the model presented in Sect. 2 is checked. The initiation threshold is studied first through Brazilian test simulation. In order to validate the crack propagation threshold, crack propagation in a numerical sample is simulated with boundary conditions corresponding to a sandwiched beam test. In each simulation, the characteristics used to describe the studied rock are issued from an experimental campaign.

The study is performed on rock samples from the Weyburn site (Canada). The latter is considered as a demonstration site for $CO_2$ storage (Preston et al. 2005). The International Energy Agency Green House Gas (IEAGHG) Weyburn-Midale $CO_2$ storage and monitoring project was designed to assess the technical feasibility of $CO_2$ geological storage at large scale. The Weyburn and Midale oil fields are located near Midale in Saskatchewan State. Various enhanced oil recovery (EOR) techniques were used before the introduction of $CO_2$ for EOR in 2000. The rock samples were extracted from a depth of 1300 m. They are located in a particular geological layer called Lower Watrous. Lower Watrous is considered as a potential caprock for $CO_2$ storage in the Weyburn site.



**Fig. 1** Caprock sample 86 mm in diameter for a length of 180 mm

The studied rock has a complex lithology. It is a clay-rich rock with embedded grains that are mostly made of the lutites size (i.e., a diameter less than 62.5 μm (Le Nindre and Gauss 2004). The samples have a diameter of 86 mm for a length of 2.0–2.4 times their diameter (Fig. 1). Even if the studied rock has a fine microstructure, it contains mineral inclusions (made of quartz). Their diameter can reach few tenths of millimeters (Fig. 1).

The microstructure is shown in Fig. 2. It is made of clastic and granitic grains embedded in a clay–dolomitic matrix as shown in Fig. 2a. The samples also contain quartz inclusions at a higher scale; a part of an inclusion is shown in Fig. 2b. Two different scales can thus be distinguished, namely the scale of the clay matrix and that of quartz inclusions, which provide a heterogeneity at a larger scale. The material has a random porosity. The average volume fraction is 4 % (Le Nindre and Gauss 2004).

The Young's modulus and Poisson's ratio are identified via compressive tests shown in Fig. 3a. The blue lines in sub-Fig. 3b, c represent the changes in axial and radial strains measured using strain gauges under an evolving axial stress, respectively. The slope of the black line in Fig. 3b is used to calculate the Young's modulus, and the slope of the black line in Fig. 3c to evaluate the Poisson's ratio. The identified Young's modulus is equal to 16 GPa, and the Poisson's ratio is equal to 0.15. As it can be seen in Fig. 3b, it can be considered that the studied rock, as other geomaterials, exhibits a brittle behavior under unconfined compressive loading.

### 3.1 Crack Initiation

In this section, the behavior of the studied rock in terms of crack initiation in mode I is first characterized considering a Weibull model. A two-parameter Weibull model is selected to describe the behavior of the rock samples at failure. The Weibull parameters are determined using three-point flexural and Brazilian tests, thereby providing two different scales of
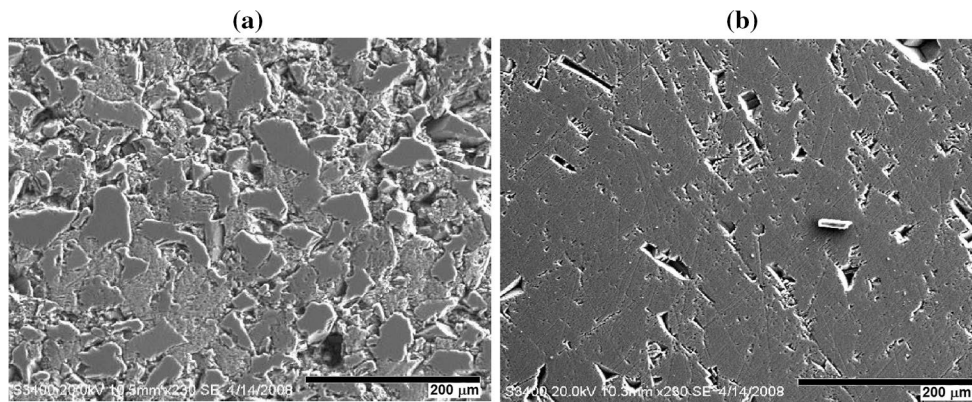
**Fig. 2** **a** Grains in clay–dolomitic matrix. **b** Quartz mineral inclusion at the same scale
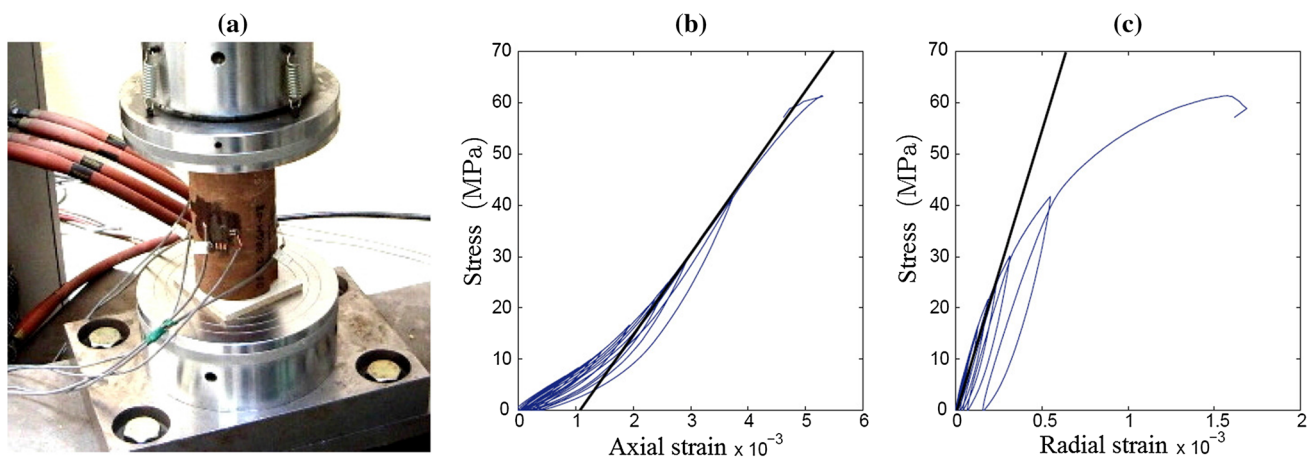


**Fig. 3** **a** Compression test. Change in axial **b** and radial **c** strains measured using strain gauges under an evolving axial stress

effective volumes. Then, the ability of the numerical model to properly describe crack initiation is studied by modeling Brazilian tests.

### 3.1.1 Identification of Weibull Parameters

The Weibull parameters are identified through an experimental campaign based on three-point flexural and Brazilian tests. The identification method (Da Silva et al. 2004) is such that it allows results issued from the two types of tests to be considered at the same time. Thirty three-point flexural tests and 34 Brazilian tests were performed. For the three-point flexural tests the sample dimensions are $h \approx 18.75$ mm, $b \approx 18.75$ mm and $L = 75.0$ mm. For the Brazilian tests, the sample radius is $R \approx 43$ mm and its length is $L \approx 80$ mm. For each broken sample, a maximum principal stress $\sigma_f$ is calculated from the actual sample dimensions and load to failure. In order to identify only one set of Weibull parameters that suits both series of tests, a Weibull stress (Beremin 1983; Da Silva et al. 2004) is introduced for each broken sample

$$\sigma_w = \sigma_f \left( HV\lambda_0 \right)^{\frac{1}{m}} \tag{11}$$

where $H$ is the stress heterogeneity factor, and $V$ the sample volume that are equal to $H_{br}$ and $V_{br}$ for the Brazilian tests and to $H_{fl}$ and $V_{fl}$ for the three-point flexural tests. Therefore, the Weibull parameters, $m$ the Weibull modulus and $\sigma_0^m / \lambda_0$ the scale parameter, can be deduced from the Weibull stresses in ascending order $\sigma_{wi}$. The linear regression method can be used to identify the parameters as it is relevant when few experimental data are available (Gosh 1999; Wu et al. 2006). The principle is to assign to each Weibull stress $\sigma_{wi}$ a failure probability $P_{Fi}$ such that

$$P_{Fi} = \frac{i}{n_s + 1} \tag{12}$$

where $n_s$ is the total number of samples. It can be deduced from the Weibull model that

$$\ln\left[-\ln\left(1 - P_{Fi}\right)\right] = m\left[\ln(\sigma_{wi}) - \ln\left(\sigma_0\right)\right]; \tag{13}$$
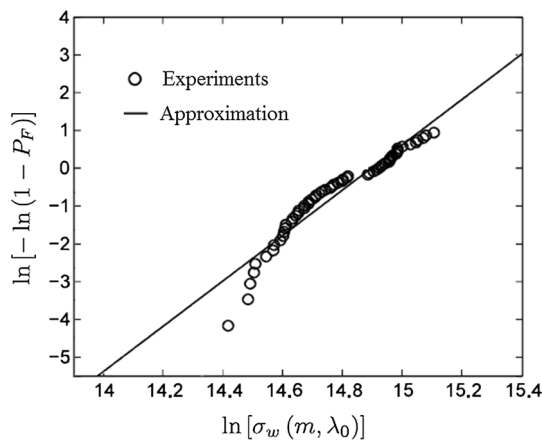
**Fig. 4** Modified Weibull diagram for the identification of parameters based on three-point flexural and Brazilian tests

therefore, the Weibull parameters can be calibrated from an iterative least squares analysis (Da Silva et al. 2004). The Weibull diagram is shown in Fig. 4. The identified Weibull modulus is $m = 6.0$, which corresponds to a clearly heterogeneous material; it is in the typical range of values for rocks (i.e., $3 \leq m \leq 9$). As it can be seen in Fig. 4, there is a good agreement between experimental data and the model.

It is to be noted that the use of a two-parameter Weibull model leads to a conservative estimation of failure probability for the lowest stresses as no threshold is considered.

### 3.1.2 Validation of Initiation Modeling

In order to validate the initiation threshold, numerical modeling of Brazilian tests is performed. The rock samples are modeled in a 2D setting under plane strain hypothesis by disks that have a radius of $R = 43$ mm. The rock parameters are those identified previously. For the computation of the initiation threshold the element volume is required. In the present case the length of the specimens $L = 85$ mm is considered as the thickness of the element. The Weibull modulus is $m = 6.0$ and the scale parameter is $\sigma_0^m / \lambda_0 = 7.3 \times 10^{35}$ Pa$^m$m$^3$. The characteristic

length is considered as $\ell_c = 2$ mm to be small enough to allow for a relevant description of the stress state in the numerical specimen with the regularized stress. A characteristic length of $\ell_c = 2$ mm implies that initial cracks (i.e., initial defects) are smaller than 4 mm, which is a reasonable hypothesis. The nominal initiation stress is $\sigma_{\ell_c} = \sigma_0 / (\lambda_0 \ell_c^3)^{1/m} = 21.2$ MPa. The numerical model is shown in Fig. 5.

The displacements are zero on the bottom of the structure. For the highest point, the horizontal displacements are zero and a vertical force is applied. The mesh is shown in Fig. 5a. In Fig. 5b the initiation thresholds obtained for each element of one numerical sample are mapped. The initiation threshold for each element is obtained considering its size and following a random selection of an initiation probability from a uniform distribution using Eq. (2). This procedure results in a scattered map ranging from 3.6 MPa to 40 MPa. Only the lowest initiation thresholds have an influence on the results as the potential initiation sites. In the simulations performed with Code_Aster (2010), the regularized stress field tends to lead to crack initiation in the middle of the specimen, which is consistent with experimental observations.

The theoretical failure probability reads

$$P_F = 1 - \exp\left[-\left(\frac{\sigma_w}{\sigma_0}\right)^m\right]. \tag{14}$$

One hundred simulations were performed to obtain one hundred Weibull stresses $\sigma_{wi}$. For each Weibull stress $i$ a failure probability is defined $P_{Fi} = i/(n + 1)$. The results of numerical simulations, analytical model [Eq. (14)] and experiments are plotted in Fig. 6.

The results provided by the three approaches are consistent. Only small differences are observed for low probabilities. This difference is due to the cutoff of the lowest part of the Weibull distribution associated with initial defects due to the consistency condition [Eq. (10)]. In the present case, the consistency condition leads to the hypothesis that initial cracks are smaller than 4 mm. It appears that for low probabilities the numerical model

**Fig. 5** Mesh **a** and crack initiation threshold **b** for the upper half of the model used to simulate Brazilian tests
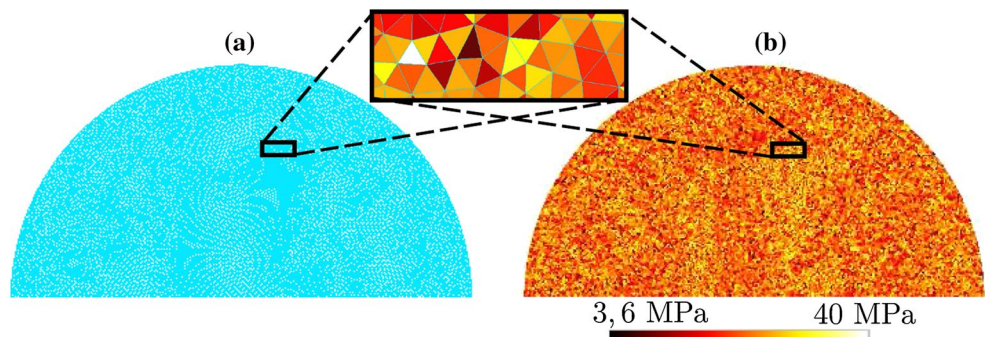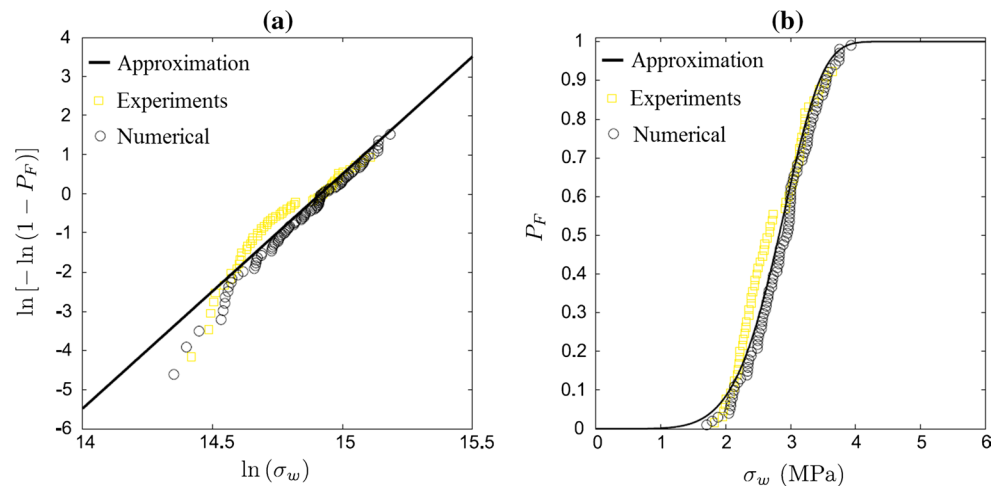
**Fig. 6** Modified Weibull diagram **a** and failure probability $P_F$ as functions of the Weibull stress $\sigma_w$ **b** for the numerical, analytical and experimental approaches

is closer to the experimental results than the analytical model.

## 3.2 Crack Propagation

The toughness describes the material ability to resist crack propagation. In linear elastic fracture mechanics, the fracture toughness is usually compared to stress intensity factors to predict crack propagation. The material toughness can be identified from three-point flexural tests performed on notched specimens even if in this context crack propagation is unstable for brittle materials. An analytical solution can be used to link the failure load with the material toughness and the notch length (Murakami 1987). Pre-cracking can be performed with sandwiched beam tests that allow for stable crack propagation (Srawley 1976; Nose and Fuji 1988; Lawn 1993). Digital image correlation (DIC) (Sutton et al. 2009; Hild and Roux 2006) is an experimental method that allows displacement fields to be measured and that can be used for detecting and quantifying crack initiation and propagation (Roux and Hild 2006). Specific DIC features have been developed in order to calculate stress intensity factors (Forquin et al. 2004; Roux and Hild 2006). They will be used hereafter. The material toughness is measured with a two-step experimental campaign consisting of first pre-cracking the sample (here with an SB configuration) and then loading the pre-cracked sample in three-point flexure up to failure.

### 3.2.1 Image-Based Identification of Fracture Toughness

The failure of a brittle material tends to be very sudden because it commonly results from unstable crack propagation. Several methods exist to perform sample pre-cracking (Nose and Fuji 1988; Lawn 1993). One solution is to load the specimen in such a way that crack initiation and stable propagation are possible [*e.g.,* sandwiched beam (SB) test (Pancheri et al. 1998)]. The SB test uses three beams,
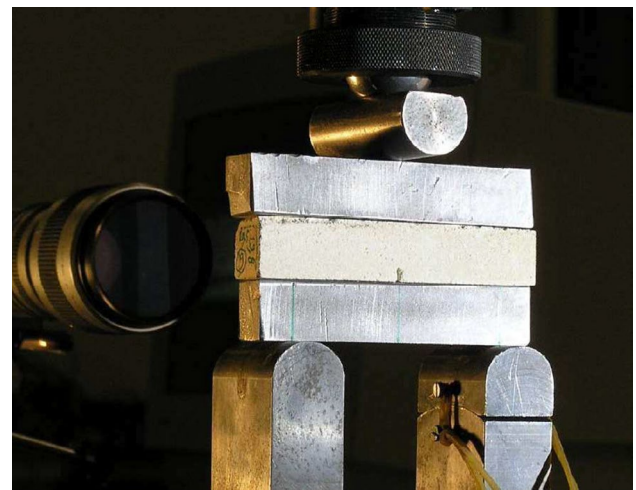


**Fig. 7** Sandwiched beam test in which the rock sample is loaded with the two aluminum alloy beams

namely the central beam to be pre-cracked and two identical beams made of a more rigid material as shown in Fig. 7.

In the present study, the lower and upper beams are made of aluminum alloy and have a Young's modulus of 70 GPa. Each beam has a thickness of 18.75 mm; the central beam has a height of 18.75 mm, and the lower and upper ones a height of 20.00 mm. All the beams have a length of more than 75.0 mm. Crack initiation and location can be detected with the use of DIC (Fig. 8). In the present case, a global DIC code with Q4 quadrilaterals is utilized (Besnard et al. 2006). From the measured displacement field, the mean infinitesimal strains per element are computed. The maximum eigen strain field exhibits a very localized region corresponding to the presence of a crack.

At this stage of the experimental process, the material arrest toughness can be deduced from the measured displacement fields (Roux and Hild 2006) under the assumption that the crack is propagating. After sample pre-cracking,
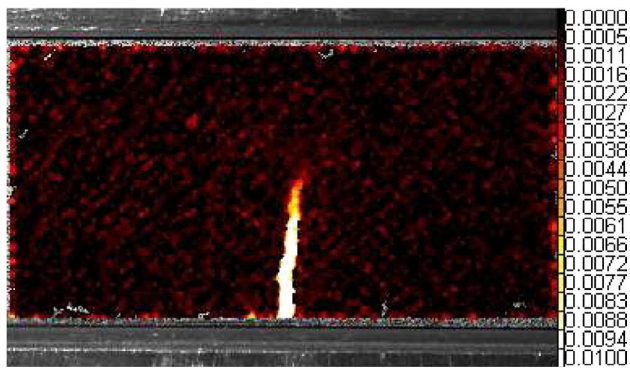
**Fig. 8** Maximum eigen strain field in sample no. 2 when pre-cracked. The physical size of 1 pixel is $\approx 20.7\,\mu m$



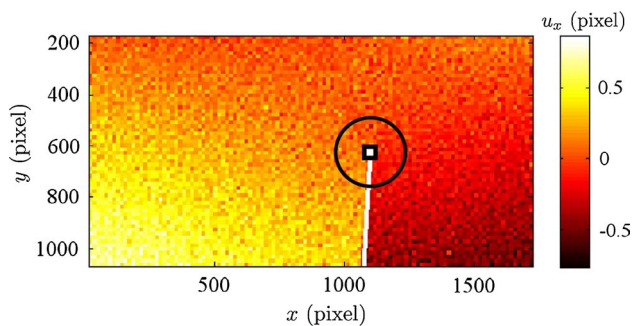**Fig. 10** Change in mode I stress intensity factor with applied load



**Fig. 9** Measured horizontal displacement field (expressed in pixels) when rigid body translations have been removed. Pre-cracked sample (no. 2) submitted to a load $F = 350\,N$ in three-point flexural test. The physical size of 1 pixel is $\approx 20.3\,\mu m$

three-point flexural tests are performed for toughness identification with the use of DIC. Figure 9 shows the results for sample no. 2 in three-point flexure for an applied load of $F = 350\,N$. The horizontal displacement field is shown after rigid body translation removal. The crack tip location used for the post-processing step is plotted in white. The area in black is used for the post-processing based on a comparison between measured displacement field and Williams' series of the displacement field close to the singularity (Roux and Hild 2006).

The stress intensity factor is estimated for different loading levels in order to obtain a better estimation of the fracture toughness as shown in Fig. 10. Knowing the failure load $F_c = 368\,N$ for the considered sample, the fracture toughness is estimated by linearly extrapolating the stress intensity factor with the applied load. For the present test a fracture toughness of $1.04\,MPa\sqrt{m}$ is obtained.

Five samples (no. 1–5) have led to fracture toughness identification for both steps of the experimental campaign. The results are summarized in Table 1. It is worth noting that the residual error in terms of displacement given for
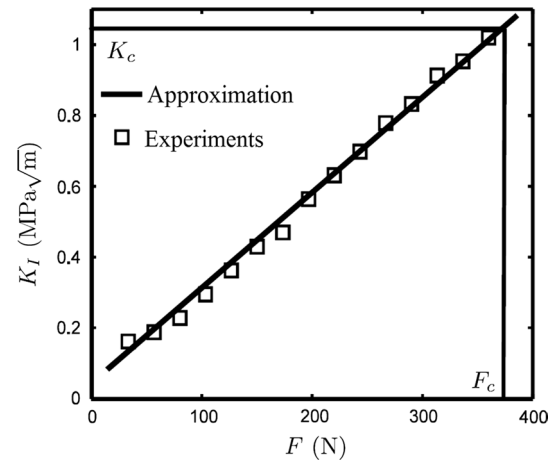
the identification corresponding to the maximum load is low compared with the displacement uncertainty levels (i.e., 0.02 pixel). Therefore, the estimated stress intensity factors are deemed trustworthy. The mode I stress intensity factors are scattered from $K_I(a) = 0.11\,MPa\sqrt{m}$ to $K_I(a) = 0.32\,MPa\sqrt{m}$ for the pre-cracking phase, and between $K_I(b) = 0.16\,MPa\sqrt{m}$ and $K_I(b) = 1.04\,MPa\sqrt{m}$ for the subsequent three-point flexural tests. The observed scatter again reflects the material heterogeneity.

Despite scattered results, two clear tendencies can be pointed out. First, the mode II stress intensity factors are significantly lower than mode I levels. The mode II stress intensity factors are relatively higher for the SB tests as shown by the values $r_K = K_{II}/K_I$. It means that the cracking mode is mode I dominant for the three-point flexural tests. This result can be explained by the confinement induced by the use of the metallic beams. Second, the stress intensity factors estimated for both tests are different with averages of $K_I(a) = 0.21\,MPa\sqrt{m}$ and $K_I(b) = 0.55\,MPa\sqrt{m}$. This tendency (of finding lower values for the pre-cracking tests) is observed for each sample. It can be explained by the fact that the stress intensity factors identified in three-point flexural tests are associated with crack propagation inception, whereas those determined with SB (pre-cracking) tests correspond to crack arrest. Given the experimental scatter, it is chosen to select a single value $K_c = 0.21\,MPa\sqrt{m}$ as a conservative estimate.

### 3.2.2 Validation of Crack Propagation Modeling

In order to validate the crack propagation threshold introduced in Sect. 2, the results obtained with DIC are compared with those issued from numerical simulations. An SB test is modeled. The DIC results are based on a spatial discretization of $8 \times 8$ pixel elements (1 pixel $\approx 20.7\,\mu m$). The

**Table 1** Toughness results for sandwiched beam tests (a) and three-point flexural tests (b) for the five studied samples

| Sample | 1 | 2 | 3 | 4 | 5 | Average |
|---|---|---|---|---|---|---|
| $K_I$ (MPa$\sqrt{m}$) (a) | 0.13 | 0.31 | 0.11 | 0.32 | 0.19 | 0.21 |
| $K_{II}$ (MPa$\sqrt{m}$) (a) | 0.07 | 0.12 | 0.05 | 0.20 | 0.11 | 0.11 |
| $r_K = K_{II}/K_I$ (a) | 0.54 | 0.39 | 0.45 | 0.62 | 0.58 | 0.52 |
| Error (pixel) (a) | 0.03 | 0.02 | 0.02 | 0.02 | 0.02 | 0.02 |
| Resolution (μm/pixel) (a) | 20.5 | 20.7 | 20.7 | 20.6 | 20.8 | 20.7 |
| $K_I$ (MPa$\sqrt{m}$) (b) | 0.44 | 1.04 | 0.16 | 0.40 | 0.72 | 0.55 |
| $K_{II}$ (MPa$\sqrt{m}$) (b) | 0.07 | 0.13 | 0.04 | 0.02 | 0.11 | 0.07 |
| $r_K = K_{II}/K_I$ (b) | 0.16 | 0.13 | 0.25 | 0.05 | 0.015 | 0.13 |
| Error (pixel) (b) | 0.02 | 0.09 | 0.02 | 0.02 | 0.04 | 0.04 |
| Resolution (μm/pixel) (b) | 20.1 | 20.3 | 20.3 | 20.6 | 20.4 | 20.3 |

measured displacements on the external boundary of the analyzed area are used as (Dirichlet) boundary conditions of the numerical model. In the present case, the external boundary is a rectangle and the finite element models used in the numerical computations are based on the same mesh used for DIC purposes. With such setting there is no need to model friction between the different beams of the SB test, and realistic boundary conditions are prescribed as measured via DIC. The crack initiation threshold is uniform and considered high enough in the modeled domain, $S_i = 10$ MPa to ensure that crack initiation appears at the right location, which is induced by the displacement loading on the bottom face. The high horizontal displacement gradient due to the initiated crack leads to a loading that induces a very significant local increase in the regularized stress, thereby initiating the crack in the numerical model. To describe crack propagation a fracture toughness of $K_c = 0.21$ MPa$\sqrt{m}$ is considered (see above).

The horizontal displacement fields measured from an experiment and simulation are shown in Fig. 11 together with the damage field at the end of the numerical computation. The results of the numerical computation are in good agreement with the experimental observations. In both cases the crack length is of the same order. A difference is observed concerning the crack orientation. For the numerical computation, the crack orientation has an angle of 3° with the vertical axis at initiation. After initiation, the crack propagation direction changes and tends to be inclined by 30°. For the experimental results, the crack orientation is of 7° for most of the propagation and tends to turn at the end of the experiments. This difference in terms of orientation is not surprising considering the applied load on the lower boundary. The displacement field used as a boundary condition in the computation does exhibit a significant gradient at the crack base not only for the horizontal value but also for the vertical one leading to a mode II loading of the crack in the 2D simulation. Therefore, it is relevant that the crack tends to be inclined in the simulation.

A major difference between the experiment and the simulation is that the experiment is performed on a 3D sample and that the crack propagation during the experiment is indeed related to a 3D displacement field. The displacement estimated through DIC at the surface could be only partially representative of the 3D displacement field. Therefore, the observed gradient of vertical displacement at the crack base could only concern the vicinity of the surface of the observed specimen, leading to a less inclined crack in the experiment than in the simulation. Moreover, Lower Watrous rock presents a slight elastic anisotropy as most sedimentary rocks. This stiffness anisotropy may also affect the crack propagation orientation.

## 4 Conclusions

The fracturing of clay-rich rock samples has been studied in both experimental and numerical ways. The samples have been extracted from the Weyburn site (Canada). An extensive experimental campaign enabled for the identification of elastic parameters thanks to uniaxial compression tests. Weibull parameters were determined via Brazilian and three-point flexural tests. They allow crack initiation to be described in a probabilistic framework. Sandwiched beam and single edge cracked beam tests enabled the toughness at crack arrest and propagation inception to be studied thanks to digital image correlation. The toughness is the key property to analyze crack propagation. Such data are quite unique for this type of rocks.

The capacities of a probabilistic nonlocal damage model to describe crack initiation and propagation are analyzed through the comparison of experimental and numerical results. Each of these mechanisms has been associated with an experimental process. Numerical simulations of Brazilian tests are performed in order to evaluate the numerical model ability to reproduce crack initiation. A consistent description of the tests with a Weibull law shows that initiation is dominant in such situations

**Fig. 11** **a** Horizontal measured displacement field. **b** Simulated displacement field. **c** Damage field for sample no. 2 in the sandwiched beam test
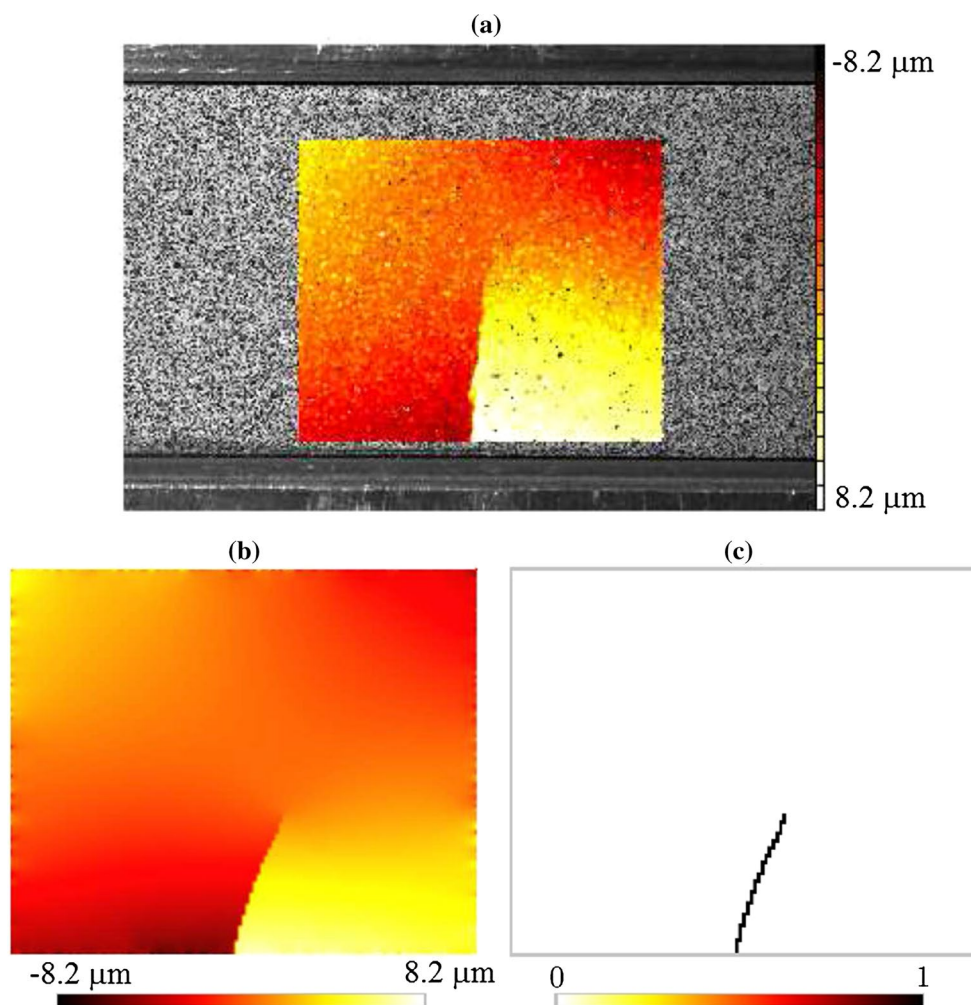


(i.e., the weakest link hypothesis is satisfied). Simulation of crack propagation in a numerical model loaded with boundary displacements issued from digital image correlation measurements is also performed and yields consistent results in comparison with experiments. The crack length estimation is relevant, and the crack orientation estimation is slightly different from the experiment.

To enhance the results, an extensive study of the effect of mixed-mode loading and especially on the effect of mode II loading could be interesting. Further, no scatter in terms of fracture toughness was considered. This may also change the actual path of the crack. Yet, it appears that the numerical model is able to provide a good prediction of crack propagation and especially of its length. However, differences in terms of crack orientation between experiments and simulations are observed. This could be explained by 3D effects that are not considered in the 2D simulations, and elastic anisotropy of the studied rock.

## References

Baecher GB, Einstein HH (1981) Scale effect in rock testing. Geophys Res Let 8:671–674

Baghbanan A, Lanru J (2007) Hydraulic properties of fractured masses with correlated fracture length and aperture. Int J R Mech Min Sci 44:704–719

Bažant Z, Belytschko TB (1985) Wave propagation in strain-softening bar: exact solution. J Eng Mech 111:381–389

Bažant ZP, Pijaudier-Cabot G (1988) Nonlocal continuum damage, localization instability and convergence. J Appl Mech 55:521–539

Beremin FM (1983) A local criterion for cleavage fracture of a nuclear pressure vessel steel. Metall Trans 14:2277–2287

Besnard G, Hild F, Roux S (2006) "Finite-element" displacement fields analysis from digital images: application to Portevin-Le Chatelier bands. Exp Mech 46:789–804

Bush AJ (1976) Experimentally determined stress-intensity factors for single-edge-crack round bars in bending. Exp Mech 16:249–257

Code_Aster (2010). EDF R&D. http://www.code-aster.org. Accessed 1 June 2010

Da Silva ACR, Proença SPB, Billardon R, Hild F (2004) Probabilistic approach to predict cracking in lightly reinforced microconcrete panels. J Eng Mech 130:931–941

De Borst R, Sluys LJ, Muhlaus HB, Pamin J (1993) Fundamental issues in finite element analysis of localization of deformation. Eng Comput 10:99–121

Forquin P, Rota L, Charles Y, Hild F (2004) A method to determine the macroscopic toughness scatter of brittle materials. Eur J Mech A Solids 125:171–187

Funatsu T, Seto M, Shimada H, Matsui K, Kuruppu M (2004) Combined effects of increasing temperature and confining pressure on the fracture toughness of clay bearing rocks. Int J R Mech Min Sci 41:927–938

Gosh A (1999) A FORTRAN program for fitting Weibull distribution and generating samples. Comput Geosci 25:729–738

Guy N (2010) Modélisation probabiliste de l'endommagement des roches : application au stockage géologique du $CO_2$. Ph.D. thesis, Ecole Normale Supérieure de Cachan

Guy N, Seyedi D, Hild F (2010) Hydro-mechanical modelling of geological $CO_2$ storage and the study of possible caprock fracture mechanisms. Georisk 4:110–117

Guy N, Seyedi D, Hild F (2012) A probabilistic nonlocal model for crack initiation and propagation in heterogeneous brittle materials. Int J Numer Methods Eng 90:1053–1072

Hild F, Roux S (2006) Digital image correlation: from displacement measurement to identification of elastic properties—a review. Strain 42:69–80

Jobmann M, Wilsnack T, Voigt HD (2010) Investigation of damage induced permeability of Opalinus clay. Int J R Mech Min Sci 47:279–285

Kanninen MF, Brust FW, Ahmad J, Abou-Sayed IS (1982) The numerical simulation of crack growth in weld-induced residual stress fields. In: Kula E, Weiss V (eds) Residual stress and stress relaxation. Plenum Press, New York, pp 975–986

Lasry D, Belytschko T (1988) Localization limiters in transient problems. Int J Solids Struct 24:581–597

Lawn BR (1993) Fracture of brittle material. Cambridge University Press, Cambridge

Le Nindre YM, Gauss I (2004) Characterisation of the lower watrous aquitard as major seal for $CO_2$ geological sequestration. In: 7th International Conference on Greenhouse Gas Control Technologies, Vancouver, Canada, 5–9 Sept

Lorentz E, Benallal A (2005) Gradient constitutive relations: numerical aspects and application to gradient damage. Comput Methods Appl Mech Eng 194:5191–5220

Lyakhovsky V, Hamiel Y, Ben-Zion Y (2011) A non-local visco-elastic damage model and dynamic fracturing. J Mech Phys Solids 59:1752–1776

Murakami Y (1987) Stress intensity factors handbook. Pergamon Press, Oxford

Nose T, Fuji T (1988) Evaluation of fracture toughness for ceramics materials by a single-edge-precracked-beam method. J Am Ceram Soc 71:328–333

Ouchterlony F (1988) ISRM commission on testing methods; suggested methods for determining fracture toughness of rock. Int J R Mech Min Sci 25:71–96

Pancheri P, Bosetti P, Dal Maschio R, Sglavo VM (1998) Production of sharp cracks in ceramic materials by three-point bending of sandwiched specimens. Eng Frac Mech 59:447–456

Peerlings RHJ, de Borst R, Brekelmans WAM, Geers MGD (1998) Gradient-enhanced damage modelling of concrete fracture. Mech Cohes Frict Mater 3:323–342

Peerlings RHJ, Geers MGD, de Borst R, Brekelmans WAM (2001) A critical comparison of non-local and gradient-enhanced softening continua. Int J Solids Struct 38:7723–7746

Pietruszczak S, Mróz Z (1981) Finite element analysis of deformation of strain-softening materials. Int J Numer Methods Eng 17:327–334

Pijaudier-Cabot G, Bažant ZP (1987) Nonlocal damage theory. J Eng Mech 113:1512–1533

Preston C, Monea M, Jazrawi W, Brown K, Whittaker S, White D, Law D, Chalaturnyk R, Rostron B (2005) IEA GHG Weyburn $CO_2$ monitoring and storage project. Fuel Process Technol 86:1547–1568

Roux S, Hild F (2006) Stress intensity factor measurements from digital image correlation: post-processing and integrated approaches. Int J Fract 140:141–157

Srawley JE (1976) Wide range stress intensity factor expressions for ASTM E399 standard fracture toughness specimens. Int J Frac 12:475–476

Sutton MA, Orteu JJ, Schreier H (2009) Image correlation for shape, motion and deformation measurements: basic concepts, theory and applications. Springer, New York

Triantafyllidis N, Aifantis EC (1986) A gradient approach to localization of deformation: I. Hyperelastic materials. J Elast 16:225–237

Weibull W (1939) A statistical theory of the strength of materials. Generalstabens Litografiska Anstalts Förlag, Stockholm

Wu D, Zhou J, Li Y (2006) Unbiased estimation of Weibull parameters with the linear regression method. J Eur Ceram Soc 26:1099–1105

Zuo JP, He-Ping X, Feng D, Yang J (2014) Three point bending test investigation of the fracture behavior of siltstone after thermal treatment. Int J R Mech Min Sci 70:133–143